# Supplementary Information for

# Core–Shell Mg–Ni Carbonate Supercapacitor Material by Concurrent Ni Recovery and $CO_2$ Mineralization

*Ying Wang[1], Xueyi Liu[1], Sebastien N. Kerisit [2] and Young-Shin Jun[1,*]*

[1]Department of Energy, Environmental & Chemical Engineering, Washington University in St. Louis, St. Louis, Missouri 63130, United States

[2]Physical and Computational Sciences Directorate, Pacific Northwest National Laboratory, Richland, WA 99352, United States

Email: ysjun@seas.wustl.edu

http://encl.engineering.wustl.edu/

*Materials Horizons*

*To Whom Correspondence Should be Addressed

Summary: a total of 13 pages including 5 notes, 9 Figures and 3 Tables

**Table S1.** Comparison of magnesite and gaspéite compositions using different methods.

| | Theoretical values | | TGA method | | XRD method | |
|---|---|---|---|---|---|---|
| **Samples** | **$MgCO_3$ (%)** | **$NiCO_3$ (%)** | **$MgCO_3$ (%)** | **$NiCO_3$ (%)** | **$MgCO_3$ (%)** | **$NiCO_3$ (%)** |
| **Mg:Ni 20:5** | 74.0 | 26.0 | 73.5 | 26.5 | 76.6 | 23.4 |
| **Mg:Ni 20:10** | 48.7 | 41.3 | 57.6 | 42.4 | 59.8 | 40.2 |
| **Mg:Ni 20:20** | 41.5 | 58.5 | 38.4 | 61.6 | 51.2 | 48.8 |

**Table S2.** Electrochemical impedance spectroscopy (EIS) simulation results for pure $NiCO_3$ and $MgCO_3$/$NiCO_3$ electrodes.

| **Parameter** | ***R1*** | ***R2*** | ***R3*** | ***Q*** | ***C*** |
|---|---|---|---|---|---|
| **pure $NiCO_3$** | 2.226 | 58710 | 172.4 | 0.00159 | 4.928E-4 |
| **$MgCO_3$/$NiCO_3$** | 2.237 | 18800 | 114.6 | 0.00193 | 6.597E-4 |

**Table S3.** Saturation ($\sigma = \ln Q/K_{sp}$) with respect to magnesite and gaspéite and pH values at $T$ = 180°C and $pCO_2$ = 100 bar.

| **Mg : Ni ratio** | **20 mM : 0 mM** | **20 mM : 5 mM** | **20 mM : 10 mM** | **20 mM : 20 mM** | **0 mM : 20 mM** |
|---|---|---|---|---|---|
| **Magnesite** | 9.46 | 9.46 | 9.44 | 9.39 | -- |
| **Gaspéite** | -- | 7.90 | 8.57 | 9.16 | 9.21 |
| **pH** | 5.76 | 5.76 | 5.76 | 5.75 | 5.76 |

**Note S1: Thermogravimetric Analysis (TGA) weight percentage calculations**

$$X + Y = 1 \qquad \textbf{Eq. S1}$$

$$1 - L = 0.478 \times X + 0.6292 \times Y \qquad \textbf{Eq. S2}$$

where $X$ was the weight percentage for gaspéite, $Y$ was the weight percentage for magnesite, and $L$ was the weight loss percentage obtained from TGA. By solving the equations above, we can derive the formulas provided in **Eqs. 5** and **6** of the main text.

**Note S2: Density Functional Theory Calculations**

Two series of calculations were performed. The first series of calculations used the PBE0 functional and aimed at determining the energy of the decomposition reaction $M\mathrm{CO_{3\,(s)}} \rightarrow M\mathrm{O_{(s)}} + \mathrm{CO_{2\,(g)}}$ for $M$ = Mg or Ni. For the solid phases, constant-pressure energy minimizations (the ionic positions, cell volume, and cell shape are allowed to relax) of the full unit cell were performed by progressively increasing the size of the $k$-point mesh until the difference between the total energies per formula unit of two consecutive energy minimizations was less than 0.01 eV. For $CO_2$, a constant-volume energy minimization was performed at the Γ point with a cubic cell with a side length of 12 Å.

The second series of calculations used the PBE-D3 functional and focused on calculating the interfacial energy between the $(10\bar{1}4)$ surfaces of magnesite and gaspéite. 2×1×5 magnesite and gaspéite slabs (20 formula units) exposing the $(10\bar{1}4)$ surface was generated from the energy-minimized full unit cells. The magnesite and gaspéite slabs had surface areas of 68.964 $Å^2$ and 68.268 $Å^2$, respectively. A magnesite-gaspéite interface was generated by joining the magnesite and gaspéite slabs using the magnesite surface area to represent magnesite serving as a substrate for gaspéite growth. A monolayer of water molecules (4 per slab face or 1 per surface cation) was

adsorbed on each face of the slabs. The results of constant-volume energy minimizations were used to calculate the magnesite-water, gaspéite-water and magnesite-gaspéite interfacial energies:

$$\alpha_i = \frac{E_{slab}^{l,m,n} - l \times E_{bulk}^{MgCO_3} - m \times E_{bulk}^{NiCO_3} - n \times E_{bulk}^{ice\ XI}}{pA} - \gamma_j \qquad \textbf{Eq. S3}$$

where *i* is *ls* (*i.e.,* liquid-substrate) for the magnesite-water interface, *lc* (*i.e.*, liquid–crystal) for the gaspéite–water interface or *sc* (*i.e.,* substrate–crystal) for the magnesite-gaspéite interface, $E_{slab}^{l,m,n}$ is the energy of a slab/interface with $l$ $MgCO_3$ units, $m$ $NiCO_3$ units, and $n$ water molecules, $E_{bulk}^{MgCO_3}$ and $E_{bulk}^{NiCO_3}$ are the bulk energies of magnesite and gaspéite, respectively, per stoichiometric unit, $E_{bulk}^{ice\ XI}$ is the bulk energy of ice XI per $H_2O$ molecule, $p$ is 2 for the magnesite–water and gaspéite–water interfaces and 1 for the magnesite–gaspéite interface, and $A$ is the surface area. Following Prange et al. (2018), ice XI was chosen as the reference phase for $H_2O$ rather than liquid water because the DFT calculations did not account for temperature.[1] Ice XI is the equilibrium structure of ice below ~70 K at ambient pressure and is the hydrogen-ordered form of ordinary ice. The term $\gamma_j$ subtracts the energy of the interfaces in the simulation cells that are not of interest, i.e., the water-vacuum interfacial energy ($\gamma_{lv}$) for the magnesite-water ($\alpha_{ls}$) and gaspéite–water interfaces ($\alpha_{lc}$) and the sum of the magnesite-water-vacuum ($\gamma_{slv}$) and gaspéite-water–vacuum ($\gamma_{clv}$) interfacial energies for the magnesite-gaspéite interface ($\alpha_{sc}$). These quantities are defined as:

$$\gamma_{lv} = \frac{E_{ML}^{n} - n \times E_{bulk}^{ice\ XI}}{2A} \qquad \textbf{Eq. S4}$$

And

$$\gamma_{slv/clv} = \frac{E_{slab}^{m,n} - m \times E_{bulk}^{MgCO_3/NiCO_3} - n \times E_{bulk}^{ice\ XI}}{2A} \qquad \textbf{Eq. S5}$$

where $E_{ML}^{n}$ is the energy of a monolayer (ML) of water molecules whose positions are those in the magnesite–water or gaspéite–water interface.

**Note S3: Galvanostatic charge–discharge (GCD) measurements**

Galvanostatic charge–discharge (GCD) measurements were carried out in a three-electrode system to assess the charge-storage behavior of the $MgCO_3$@$NiCO_3$ electrode. The composite material was used as the working electrode, with a Pt mesh counter electrode and an Ag/AgCl reference electrode in 2 M KOH. GCD curves were collected at a series of current densities to probe the rate capability of the electrode.

**Note S4: Asymmetric supercapacitor (ASC) configuration and electrochemical measurements**

In the two-electrode ASC setup, $MgCO_3$@$NiCO_3$ (R = 4 mm) and activated carbon (AC) served as the positive and negative electrodes, respectively, with 2 M KOH as the electrolyte. The energy density (E) and power density (P) were determined using **Equations S6 and S7,** based on the discharge profiles obtained from galvanostatic charge–discharge measurements.

$$E = I/2 \times Cs \times \Delta V^2 \qquad \textbf{Eq. S6}$$

$$P = E/\Delta t \qquad \textbf{Eq. S7}$$

Here, Cs represents the specific capacitance ($F/cm^2$), $\Delta V$ is the potential window (V), and $\Delta t$ is the discharge time (s). The energy density reflects the amount of energy stored per unit mass or area, while the power density indicates how quickly this energy can be delivered.

**Note S5: Electrochemical Testing of Commercial $Ni(OH)_2$ Electrode**

Electrochemical characterization, including CV, and cycling stability of the commercial $Ni(OH)_2$ electrode was performed using a three-electrode configuration, with the $Ni(OH)_2$ material as the working electrode, a Pt mesh as the counter electrode, and an Ag/AgCl electrode as the reference. All measurements were carried out in a 2 M KOH electrolyte under a scan rate of 50 mV/s.

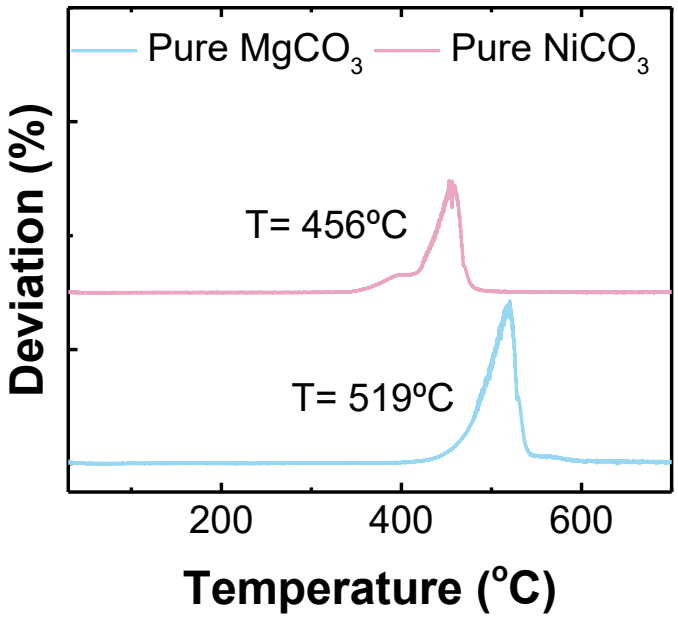


**Figure S1.** The weight deviation observed from TGA indicates that the decomposition temperatures for magnesite and gaspéite are 519°C and 456°C, respectively.

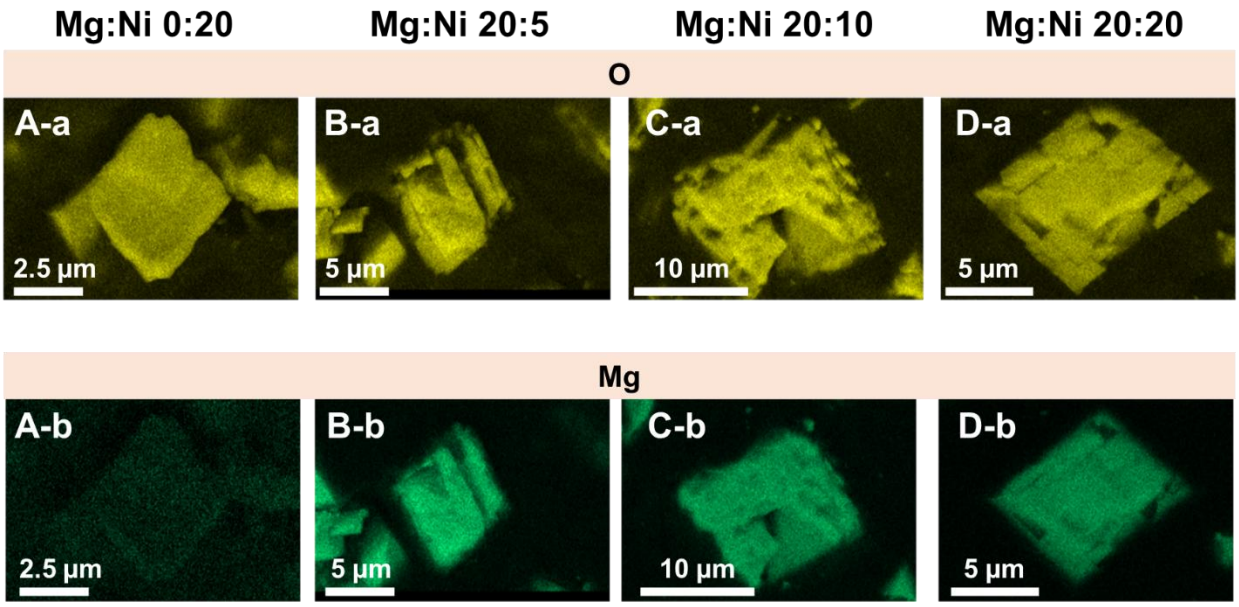


**Figure S2.** Mapping of elements O and Mg for different Mg to Ni ratio samples. The top row **(A-a, B-a, C-a, D-a)** shows the O distribution in the crystals. The bottom row **(A-b, B-b, C-b, D-b)** displays the distribution of Mg in the same crystals.

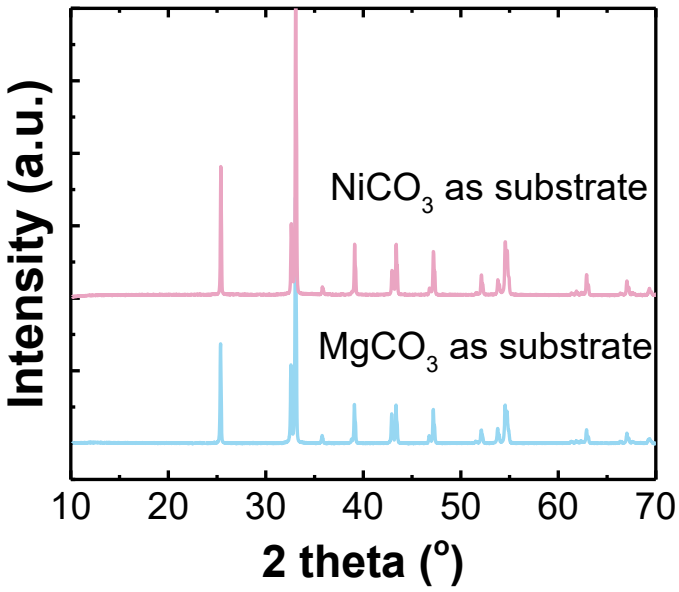


**Figure S3.** The XRD was obtained through a two-step experiment where the sequence of adding $Mg(NO_3)_2$ and $Ni(NO_3)_2$ was varied. The results showed that the final compositions were the same, regardless of the addition sequence.

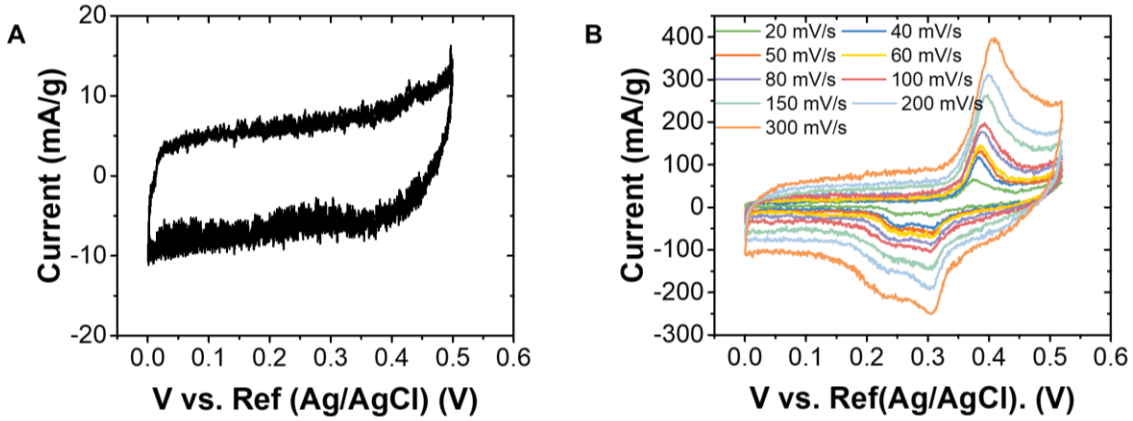


**Figure S4.** CV test for carbon papers and pure gaspéite. **(A)** The CV curves for carbon paper (control experiment). **(B)** CV curves for pure gaspéite as control material, with scan rates ranging from 20 mV/s to 300 mV/s.

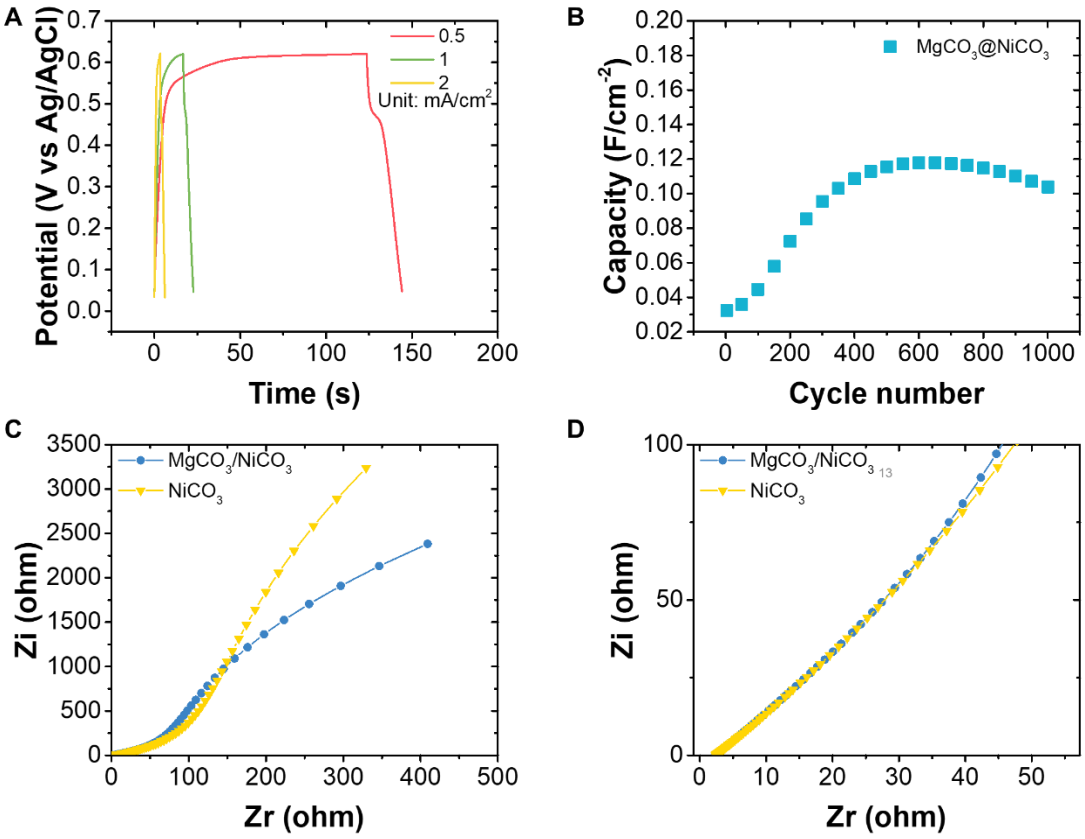


**Figure S5.** Electrochemical tests for $MgCO_3$@$NiCO_3$. **(A)** Galvanostatic charge–discharge (GCD) curves of the $NiCO_3$ electrode at 0.5, 1, 2 mA/cm$^2$; **(B)** Cycling stability of the $MgCO_3$@$NiCO_3$ electrode obtained from CV measurements at 50 mV s$^{-1}$ over 1000 cycles. **(C)** Electrochemical impedance spectroscopy (EIS) Nyquist plots of $NiCO_3$ and $MgCO_3$@$NiCO_3$ electrodes. **(D)** Enlarged high-frequency region of the Nyquist plots highlighting the solution resistance and semicircle features used in fitting with the $R_1(CR_2)(QR_3)$ equivalent circuit.

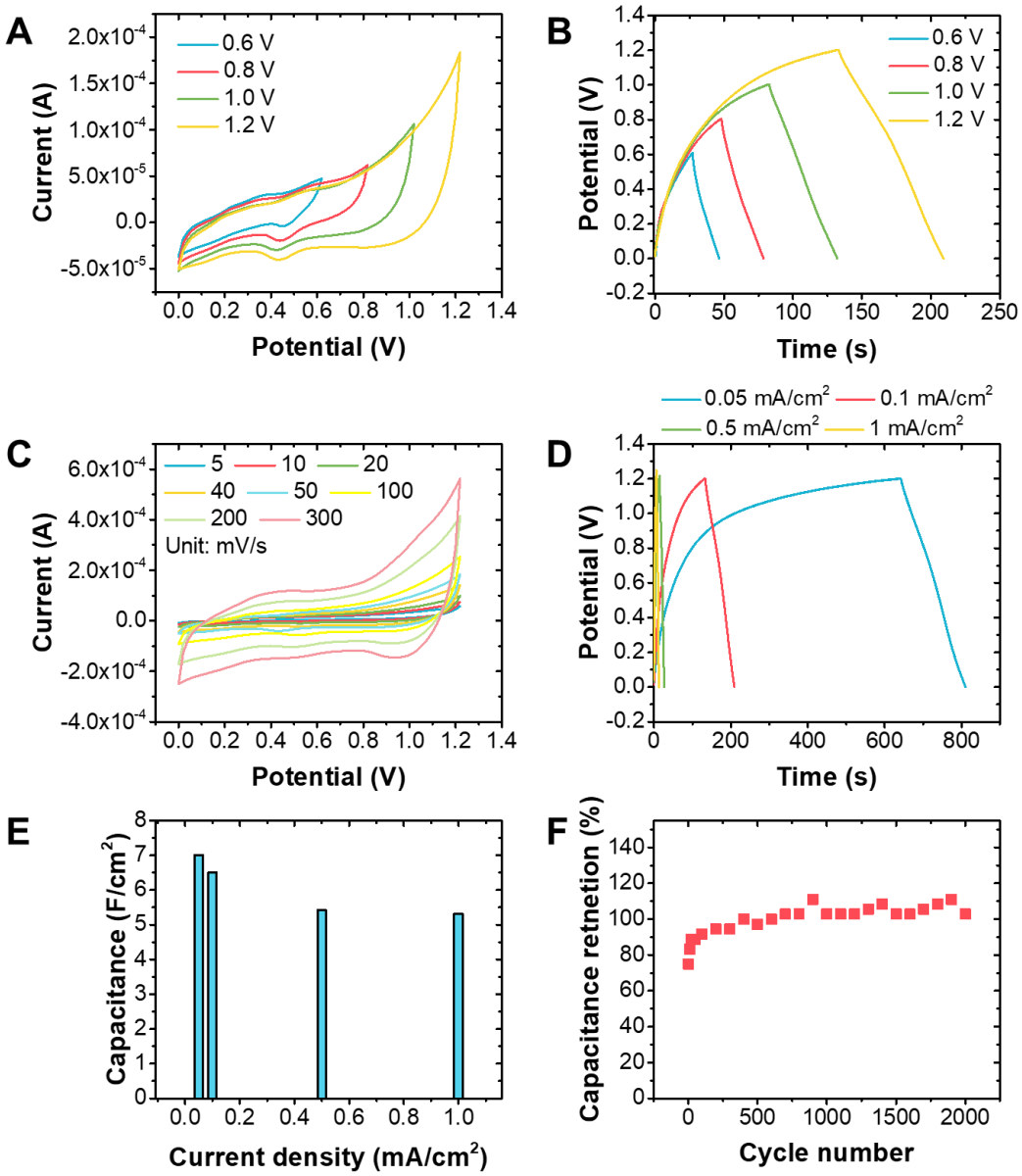


**Figure S6.** Electrochemical properties test of ASC in a two-electrode system. **(A)** CV curves of the $MgCO_3$@$NiCO_3$ // AC ASC measured at 50 mV $s^{-1}$ under different potential windows. **(B)** GCD curves of the $MgCO_3$@$NiCO_3$ // AC ASC recorded at 0.1 mA $cm^{-2}$ across various potential windows. **(C)** CV curves of the $MgCO_3$@$NiCO_3$ // AC ASC at different scan rates. **(D)** GCD curves of the $MgCO_3$@$NiCO_3$ // AC ASC at different current densities. **(E)** Specific capacitance of the ASC device as a function of current density. **(F)** Cycling performance of the ASC device over 2000 cycles at a current density of 0.1 mA $cm^{-2}$.

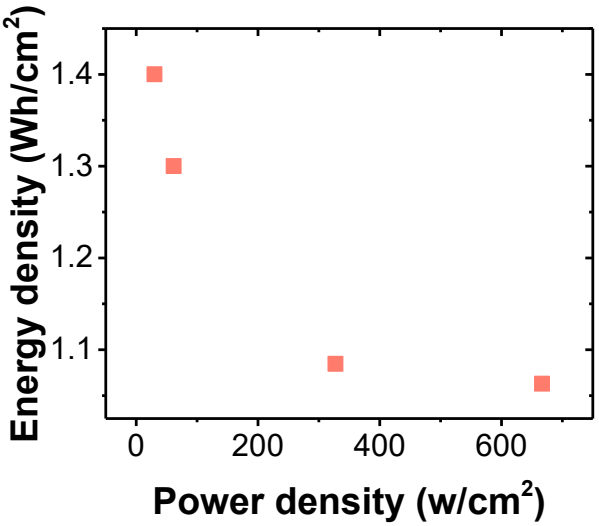


**Figure S7.** Ragone plot of $MgCO_3$@$NiCO_3$ // AC electrode.

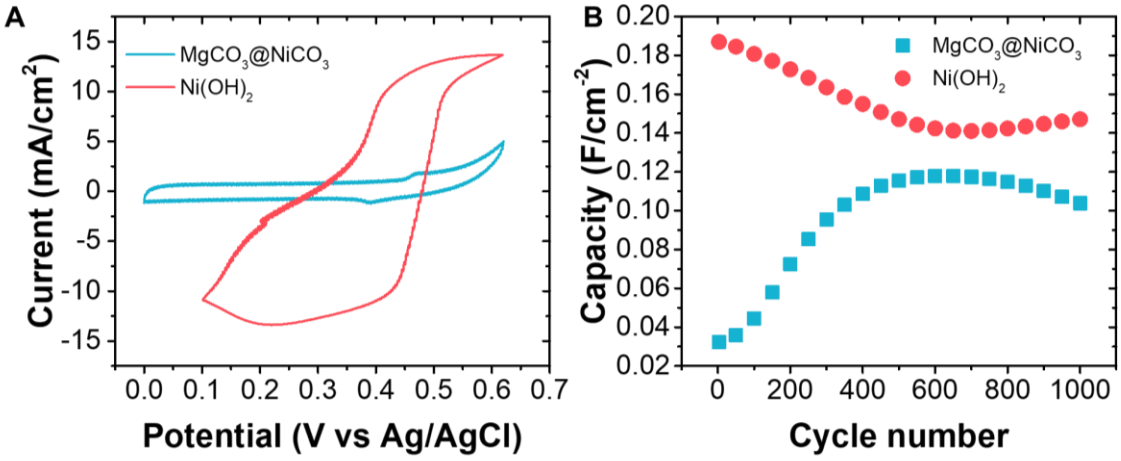


**Figure S8.** Comparison of $MgCO_3$@$NiCO_3$ and $Ni(OH)_2$. **(A)** Cyclic voltammetry (CV) curves of $MgCO_3$@$NiCO_3$ and $Ni(OH)_2$ electrodes collected at the same scan rate; **(B)** Long-term cycling stability of $MgCO_3$@$NiCO_3$ and $Ni(OH)_2$ up to 1000 cycles.

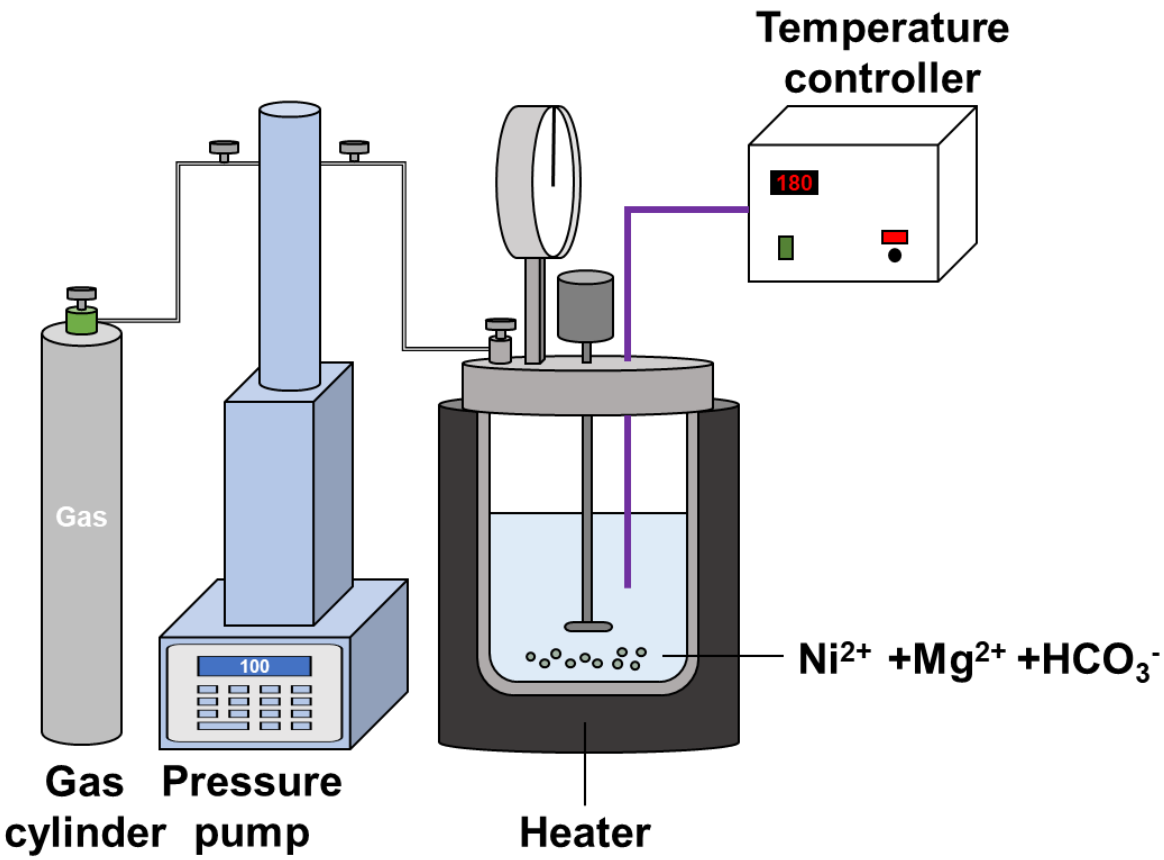


**Figure S9.** The diagram illustrates the high-temperature, high-$CO_2$-pressure (high T and P) reactor system used in our experiments. This system includes a $CO_2$ supply gas cylinder regulated by a pressure pump to maintain precise reactor pressure, and a heater controlled by an external temperature controller to achieve the required high-temperature conditions.

**Reference**

1. M. P. Prange, X. Zhang, M. E. Bowden, Z. Shen, E. S. Ilton and S. N. Kerisit, *The Journal of Physical Chemistry C*, 2018, **122**, 10400-10412.